JACS
JOURNAL OF THE AMERICAN CHEMICAL SOCIETY
Article
pubs.acs.org/JACS

Influence of Dopant Distribution on the Plasmonic Properties of Indium Tin Oxide Nanocrystals

Sebastien D. Lounis,[†,‡] Evan L. Runnerstrom,[†,§] Amy Bergerud,[†,§] Dennis Nordlund,[∥] and Delia J. Milliron*[,†,⊥]

[†]The Molecular Foundry, Lawrence Berkeley National Laboratory, 1 Cyclotron Rd., Berkeley, California 94720, United States
[‡]Graduate Group in Applied Science & Technology and [§]Department of Materials Science and Engineering, University of California, Berkeley, Berkeley, California 94720, United States
[∥]Stanford Synchrotron Radiation Lightsource, P.O. Box 20450, Stanford, California 94309, United States
[⊥]Department of Chemical Engineering, 200 E. Dean Keeton Street, The University of Texas at Austin, Austin, Texas 78712, United States

Supporting Information

ABSTRACT: Doped metal oxide nanocrystals represent an exciting frontier for colloidal synthesis of plasmonic materials, displaying unique optoelectronic properties and showing promise for a variety of applications. However, fundamental questions about the nature of doping in these materials remain. In this article, the strong influence of radial dopant distribution on the optoelectronic properties of colloidal indium tin oxide nanocrystals is reported. Comparing elemental depth-profiling by X-ray photoelectron spectroscopy (XPS) with detailed modeling and simulation of the optical extinction of these nanocrystals using the Drude model for free electrons, a correlation between surface segregation of tin ions and the average activation of dopants is observed. A strong influence of surface segregation of tin on the line shape of the localized surface plasmon resonance (LSPR) is also reported. Samples with tin segregated near the surface show a symmetric line shape that suggests weak or no damping of the plasmon by ionized impurities. It is suggested that segregation of tin near the surface facilitates compensation of the dopant ions by electronic defects and oxygen interstitials, thus reducing activation. A core−shell model is proposed to explain the observed differences in line shape. These results demonstrate the nuanced role of dopant distribution in determining the optoelectronic properties of semiconductor nanocrystals and suggest that more detailed study of the distribution and structure of defects in plasmonic colloidal nanocrystals is warranted.

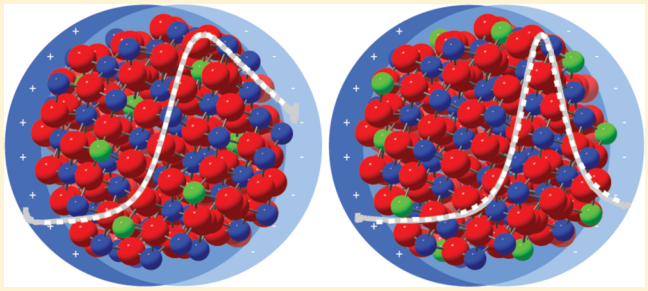

INTRODUCTION

Colloidal synthesis of nanostructures based on doped oxides has emerged in recent years as a route toward highly tunable plasmonics.[1−9] However, in contrast to their metal counterparts, there is little fundamental understanding of the optoelectronic properties of plasmonic semiconductor nanomaterials.[3,10−12] In particular, the ability to reliably control doping and, in turn, free charge-carrier concentration remains a challenge in these materials and is essential to their functionality as systems with modulable optical and electronic properties, including strong absorption and field enhancement due to localized surface plasmon resonances (LSPRs), optical transparency, and high electrical conductivity.

Of particular interest among the doped metal oxides is tin-doped indium oxide (ITO). Several colloidal syntheses have been developed for spherical ITO nanocrystals ranging in size from 3 to 15 nm and demonstrating chemically and electrochemically tunable LSPRs in the near-infrared (NIR).[6,13−16] Because of its commercial relevance as a material used in displays, thin-film solar cells, and organic electronics, thin-film ITO has been the subject of intensive applications-oriented research for decades. However, little is known about the underlying mechanisms of doping and defect formation in colloidal ITO nanocrystals, and the relationship between structural properties such as dopant distribution and compensation with the optical and electronic properties of these materials has not been explored. In addition, while detailed models have been developed to describe defect chemistry in thin film ITO,[17−20] these have not been verified in colloidally synthesized nanocrystals and are still debated even in the bulk and thin-film literature.

Herein, we investigate the relationship between the radial distribution of dopants and nanocrystal optoelectronic properties, including plasmon damping and dopant activation (i.e., the number of free electrons per tin ion). Using X-ray photo-

Received: March 12, 2014
Published: April 30, 2014

 © 2014 American Chemical Society dx.doi.org/10.1021/ja502541z | J. Am. Chem. Soc. 2014, 136, 7110−7116

electron spectroscopy (XPS) combined with careful characterization of the composition and optical properties of ITO nanocrystals, we demonstrate that nanocrystals with tin-rich surfaces exhibit reduced dopant activation. We suggest that this trend is due to the formation of electronic trap states, including those due to diffusion of compensating oxygen interstitial atoms, which can more readily form neutral complexes with tin that is situated near the nanocrystal surface. On the basis of fitting of the LSPR using the Drude model, we also demonstrate that dopant distribution has an important effect on plasmon damping in this system, leading to symmetric, narrowed LSPR line shapes in the case of surface segregated tin.

EXPERIMENTAL SECTION

ITO nanocrystals were synthesized using adaptations of methods reported in the literature. Two series of samples were made: a doping series based on ref 6 comprising crystals with fixed size and varying doping levels (see Table 1) and an activation series based on ref 14 comprising crystals with fixed size and doping, but demonstrating different degrees of dopant activation (see Table 2). The salient differences between these two synthetic methods are in the precursors (indium acetate and tin ethylhexanoate vs indium acetylacetonate and tin bis(acetylacetonate) dichloride) and ligands (oleylamine and octanoic acid vs only oleylamine), respectively. We observed large variances in dopant activation for the latter synthesis recipe.

Table 1. Sample Details for Doping Series Prepared by Synthetic Method from Reference 6

sample	size (nm)	doping (Sn cat. %)	$n_e \times 10^{21}$ (cm^{-3})	activation (n_e/C_{Sn})
D1	6.2	0.12 ± 0.1	0	
D2	6.1	2.73 ± 0.03		
D3	6.8	4.53 ± 0.55	0.913	0.67
D4	6	5.10 ± 0.57	1.03	0.67
D5	5.5	6.45 ± 0.90	1.12	0.57
D6	4.9	7.60 ± 0.80	1.0	0.43

Table 2. Sample Details for Activation Series Prepared by Synthetic Method from Reference 14

sample	size (nm)	doping (Sn cat. %)	$n_e \times 10^{21}$ (cm^{-3}) from Drude	activation (n_e/C_{Sn})
A1	9.6	5.63 ± 0.72	0.612	0.36
A2	8.7	6.97 ± 0.61	1.03	0.49
A3	10.8	6.40 ± 0.82	1.25	0.65
A4	8.5	5.34 ± 0.69	1.14	0.71

Particle size and structure were verified by transmission electron microscopy (TEM, see Figure 1a and Supporting Information) and X-ray diffraction (XRD, see Figure 1b and Supporting Information), while dopant incorporation was measured using inductively coupled plasma atomic emission spectroscopy (ICP-AES). For XPS measurements, the nanocrystals were spin-coated from a concentrated solution of 1:1 hexane/octane onto silicon substrates, yielding ~100 nm thick films. In order to facilitate quantitative interpretation of surface-sensitive spectra and limit charging, the bulky organic capping ligands on these films were then exchanged with formic acid,[21] followed by a 30 minute, 300 °C anneal in flowing argon gas to decompose the remaining organic matter.

Optical measurements were made on dilute solutions of each series in tetrachloroethylene using a UV−vis−NIR spectrometer (ASD Inc./PANalytical). All spectra were measured in transmission mode and are presented as optical extinction. These spectra were fit within a MATLAB code developed by our group[22] using an extended Drude model employing the Maxwell−Garnett effective medium approximation. This model allows extraction of free electron concentrations within each sample based on the Drude formula:

$$\omega_P^2 = \frac{ne^2}{m^*\varepsilon_0}$$

where ω_P is the bulk plasma frequency, n is the free carrier concentration, e is the elementary charge, m^* is the carrier effective mass (0.4 m_e for ITO[23]), and ε_0 is the permittivity of free space. The extracted electron concentration was in turn used to determine the dopant activation in each sample by taking the ratio of the electron concentration to the tin dopant concentration. Tin concentration was calculated on the basis of the density of ITO using the formula $C_{Sn} = 3[Sn] \times 10^{20}$ cm^{-3}, where [Sn] is the tin cation percentage, determined here by ICP-AES. Care was taken to perform Drude fitting using several randomly generated initial guesses to ensure convergence on reliable values with known error.[24]

XPS data were collected on beamline 10-1 at the Stanford Synchrotron Radiation Lightsource (SSRL). XPS samples were stored in a nitrogen glovebox at all times except briefly during transfer to the ultrahigh vacuum chamber for measurement. Energy calibration was performed relative to residual carbon 1s signal found in all samples, which was set to a binding energy of 285 eV. Background subtraction was performed using macros that were developed at SSRL within the data analysis software IGOR Pro.

Surface segregation of tin was investigated by comparing the integrated area under the background subtracted In and Sn $3d_{5/2}$ XPS peaks (Figure 2). To determine the relative tin content, the ratio of the Sn $3d_{5/2}$ peak area to the total area of both peaks was taken, scaled by the relative photoionization cross-section for each element at the given photon energy.[25] For the activation series, the tin signal was also normalized by the measured doping level from ICP-AES for each individual sample, allowing direct comparison of the dopant profile despite a small variance in doping across the series. Since the $3d_{5/2}$ peaks for both elements are close in binding energy, the error

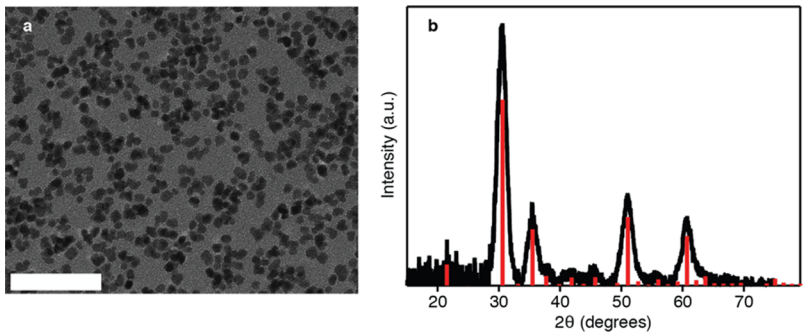

Figure 1. (a) Transmission electron micrograph (TEM) confirming pseudospherical morphology (scale bar is 50 nm) and (b) X-ray diffraction pattern confirming cubic bixbyite structure (reference pattern JCPDS 06-0416 is shown in red, data are from sample D6).

dx.doi.org/10.1021/ja502541z | J. Am. Chem. Soc. 2014, 136, 7110−7116

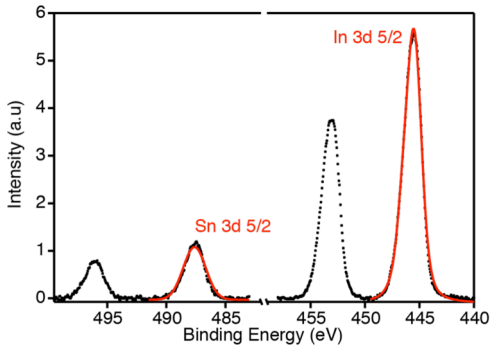

Figure 2. XPS peaks used for depth profiling (from sample D6 at 650 eV photon energy). Voigt profile fits to the data are shown in red. The area ratio of the Sn $3d_{5/2}$ peak to the total $3d_{5/2}$ signal, extracted from the fit for each peak, was used to quantify surface tin content.

introduced by differences in the escape depth of photoemitted electrons is negligible.

Due to the dependence of electron escape depth on the incident photon energy, energy-dependent XPS is an effective tool for probing the depth-dependence of elemental composition near surfaces.[26] For this reason, three photon energies, 650, 920, and 1150 eV, were used for each sample to probe the dopant depth profile. For clarity, only the results for 650 and 1150 eV, representing the most surface-sensitive and least surface-sensitive cases, respectively, are shown here. These are compared to the average compositions determined by ICP-AES.

RESULTS AND DISCUSSION

The electron concentrations and surface composition of the doping series are consistent with the reported doping behavior of thin-film ITO. As doping is increased, a strong extinction feature due to the LSPR grows in intensity, first blueshifting into the NIR and then redshifting above ~7 cat. % Sn (Figure 3a). The extracted electron concentration for nanocrystals with LSPRs peaking in the range of the spectrometer show a trend consistent with that observed for bulk and thin-film ITO, with maximum concentration in the range of 5−7 cat. % Sn. This trend can be explained by the increasing formation of irreducible Sn complexes with oxygen interstitial atoms at higher Sn concentration.[17]

The doping series shows uniform dopant distribution for low doping levels and surface segregation of tin at higher doping levels (Figure 3b). Between 0.1 and 5.1 cat. % Sn there is a linear relationship of doping with the near-surface tin content measured by XPS, with both photon energies giving approximately the same value. This indicates a uniform dopant profile, with Sn distributed evenly throughout the nanocrystal. By contrast, at 6.5 and 7.6 cat. % Sn, there is a marked increase in surface tin content, with values nearly twice the values measured by ICP-AES. At these doping levels, the measured tin content is also higher for 650 eV photons than for 1150 eV photons. These results indicate surface segregation of tin at higher doping levels, consistent with the formation of Sn-rich surfaces that has been widely documented in bulk and thin-film ITO;[27−29] similarly, aluminum-rich surfaces have been found in thin films[30] and colloidally prepared nanocrystals[8] of aluminum-doped zinc oxide.

Very similar elemental doping can also result in a wide range of free electron concentrations in ITO nanocrystals, indicating sample-to-sample differences in dopant activation. This variation can be qualitatively appreciated by the noting the large spread in LSPR frequencies observed for the activation series (Figure 4a). While these samples have approximately equal doping levels of 6.09 ± 0.64 cat. % Sn, the LSPRs show a spread of >700 nm in wavelength, exceeding any expected difference due to the small variance in doping across the sample set. Moreover, the observed shifts in the LSPR do not follow the sample-to-sample variation in doping levels, suggesting the differences in electron concentration arise instead from a compensation mechanism at work in these nanocrystals.

The dopant distribution profile of the activation series provides insight into this compensation mechanism (Figure 4b). A decreasing monotonic relationship is seen between dopant activation and surface tin content at both photon energies, and more tin signal is measured at 650 eV than 1150 eV. The latter difference is significantly larger than that for the higher doped samples in the doping series (see Figure 3b), indicating stronger surface segregation in the activation series. Moreover, all samples in the activation series have a higher surface tin content than their overall doping level, demonstrating surface segregation of Sn in even the most highly activated sample. These differences in surface segregation could arise due to the different precursors and surfactants used in each synthesis method. Indium and tin have similar reactivity when coordinated by the same type of ligands, such as the carboxylates employed in the doping series. Balanced rates of indium and tin addition reactions would explain the homogeneous distribution of tin resulting from that synthetic

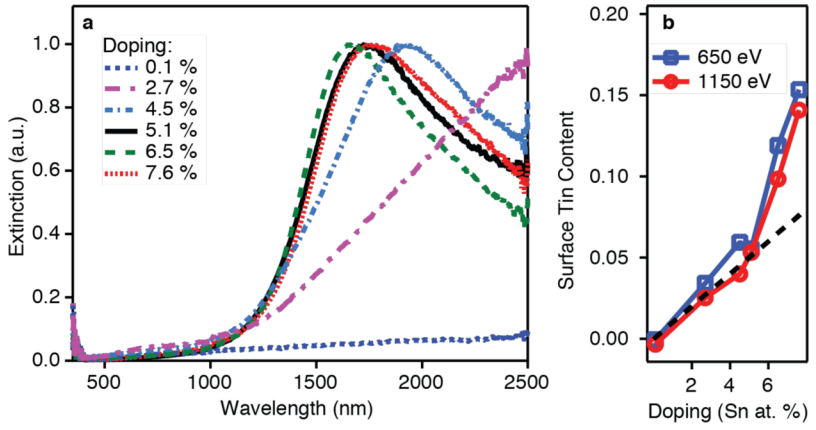

Figure 3. (a) Optical extinction and (b) XPS depth profiling versus doping for the doping series. The dotted black line in panel b shows the expected Sn/(In + Sn) ratio for a uniform doping profile.

dx.doi.org/10.1021/ja502541z | J. Am. Chem. Soc. 2014, 136, 7110−7116

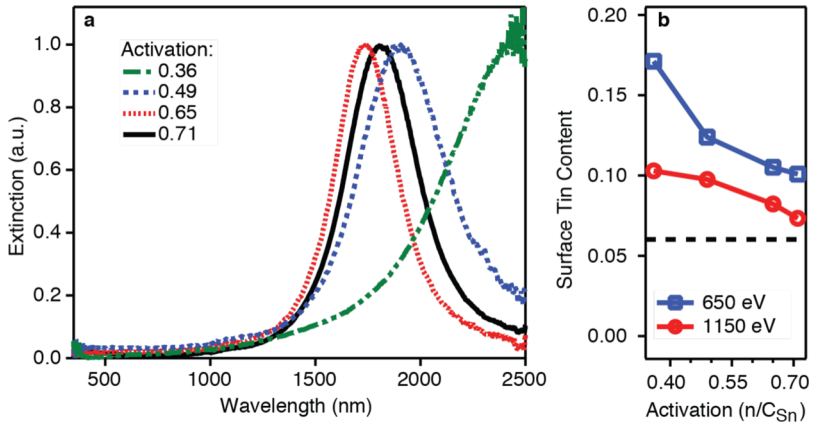

Figure 4. (a) Optical extinction and (b) XPS depth profiling versus activation for the activation series. The dashed black line in panel b corresponds to the average doping level for nanocrystals in this series.

method. However, in the reactions used to produce the activation series, the reactivity of the tin precursor ($Sn(acac)_2Cl_2$) may be reduced relative to the indium precursor ($In(acac)_3$) by the coordination of hard chloride ligands and the absence of any carboxylic acid that could the displace these ligands. Since doping kinetics depend strongly on precursor reactivity,[3] these synthetic differences are likely responsible for altering the doping profile in each set of nanocrystals.

Several detailed studies have investigated surface defects as possible charge compensating mechanisms in ITO. Early results[27] suggested the formation of alternate tin phases including SnO, SnO_2, and Sn_3O_4 based on analysis of Sn 3d XPS peak components. More recent work[28,29,31] has suggested that a combination of Sn sp hybridized surface states acting as electron traps and near-surface oxygen interstitial diffusion forming nonreducible clusters leads to a "chemical depletion region" (i.e., reduced activation) near the ITO surface. The trapping of electrons at the surface also creates a thin space-charge region that is depleted of free carriers.

We suspect a similar combination of defects to play a role in determining the activation level of our samples. The ease of oxygen interstitial incorporation in the bixbyite lattice of ITO and the low formation energy for $(Sn_{In}^{\bullet}-O_i'')^x$ complexes makes it likely that these defects play a role in our samples. Drude modeling of optical data on thin nanocrystal films also suggests a large potential barrier to interparticle electronic conduction,[24] consistent with the existence of an insulating depletion region near the surfaces of our particles and indicating that surface electron traps due to tin orbital hybridization may also play a key role as a compensating mechanism in nanocrystalline ITO. Such hybridization could be due to surface oxygen species such as hydroxide ions creating deep trap sites.

The existence of a depletion region due to electronic trap states near the ITO surface is further supported by preliminary observations of the electronic conductivity of films made from nanocrystals in each series. For an electron concentration of $\sim 1.1 \times 10^{21}$ cm^{-1}, films made from the activation series, which show significant surface segregation of tin, demonstrate conductivities that are 2−3 orders of magnitude greater than films made from the doping series (10^1 vs 10^{-2} S/cm). The same variance in conductivity holds true for films prepared as described above, as well as for unannealed films prepared from particles that are ligand-stripped with nitrosonium tetrafluoroborate ($NOBF_4$),[32] indicating that this discrepancy is inherent to the nanocrystals themselves and not due merely to differences in residual surfactants. This observation is consistent with the electrostatics of a semiconductor depletion region, in which the density of ionized dopants determines the width of the depleted layer. Thus, a nanocrystal with significant surface segregation will have a narrower depletion region than a nanocrystal with uniform doping because of the higher density of tin in the near-surface region. Since the electrostatic potential barrier between crystals mediates hopping conduction,[24] a narrower depletion region will correspond to exponentially higher conductivity.

Finally, in addition to influencing their electronic properties, the dopant profile in our ITO nanocrystals also has a strong effect on the optical line shape of the LSPR, which is determined by damping of the plasmon oscillation. The nanocrystals with uniform dopant distribution exhibit an obvious asymmetry around the LSPR peak, with a steeper change in absorbance on the high-frequency side of the peak than on the low-frequency side (Figure 3a). On the other hand, the nanocrystals with surface-segregated tin have nearly symmetric Gaussian line shape (Figure 4a).

Fitting with the Drude model allows quantitative analysis of plasmon line shape. The optical properties of a material are determined by its frequency-dependent complex dielectric function. The Drude contribution to the frequency-dependent dielectric function is given by the formula

$$\varepsilon_D(\omega) = \varepsilon_\infty - \frac{{\omega_P}^2}{\omega^2 - i\omega\Gamma(\omega)}$$

where ε_∞ is the high-frequency dielectric constant, and $\Gamma(\omega)$ is a frequency-dependent damping function. This frequency-dependence arises due to scattering of electrons off ionized impurities, which is known to be the dominant scattering mechanism in the bulk of a degenerately doped semiconductor such as ITO.[33−36] The frequency-dependent damping can be modeled using an empirical formula[37] given by

$$\Gamma(\omega) = \Gamma_L - \frac{\Gamma_L - \Gamma_H}{\pi}\left[\tan^{-1}\left(\frac{\Gamma_X}{\Gamma_W}\right) + \frac{\pi}{2}\right]$$

where Γ_L is a low-frequency damping constant, Γ_H is a high-frequency damping constant, Γ_X is the crossover frequency between the high and low regimes, and Γ_W is the width of the crossover region. Scattering off ionized impurities is characterized by the low-frequency damping constant, which is also related to the optically derived d.c. mobility of electrons within

dx.doi.org/10.1021/ja502541z | J. Am. Chem. Soc. 2014, 136, 7110−7116

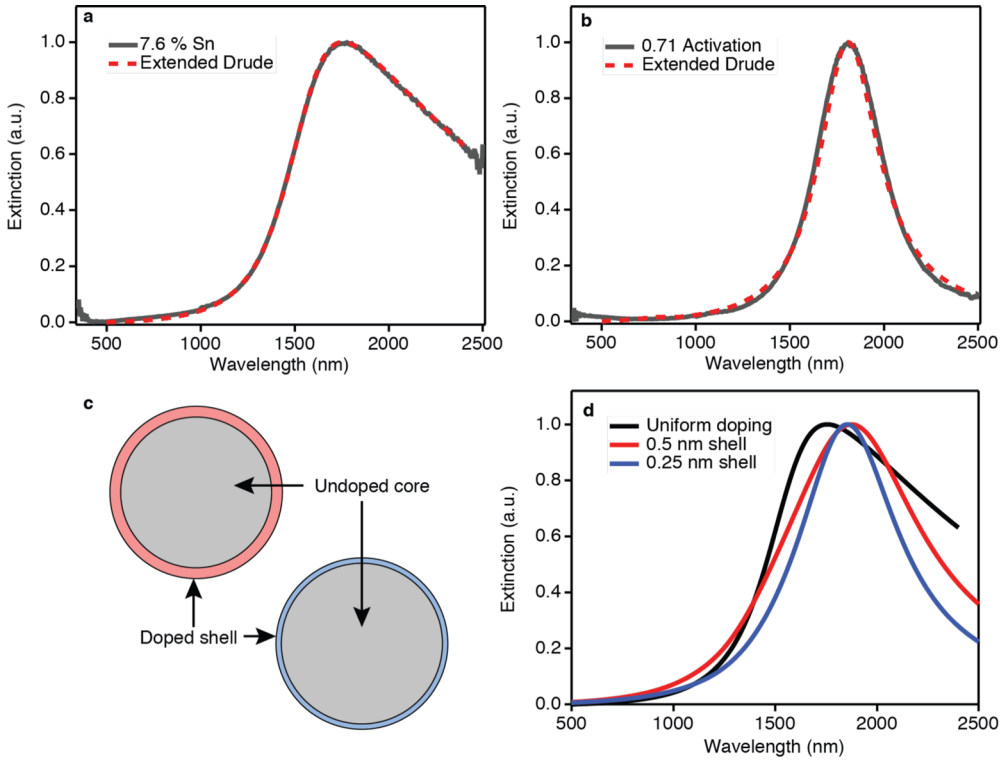

Figure 5. Optical extinction and extended Drude fit for (a) sample D6 and (b) sample A4. (c) A core–shell model with a doped shell and undoped core was employed to simulate the optical extinction of surface segregated samples (d), reproducing an asymmetric peak profile similar to that observed.

Table 3. Relevant Drude Parameters for the Doping Series

sample	ω_P (cm^{-1})	Γ_L (cm^{-1})	Γ_H (cm^{-1})	Γ_X (cm^{-1})	Γ_X (nm)	Q	Q_{Drude}
D3	13568 ± 619	8069 ± 2571	703.96 ± 426	4710.8 ± 938	2123		0.642
D4	14868 ± 229	6973 ± 698	0.001 ± 0.001	5630 ± 167.37	1776	1.77	0.831
D5	15841 ± 0.01	5585 ± 0.06	138.9 ± 0.023	6055.8 ± 0.01	1651	2.09	1.08
D6	14932 ± 0.01	5321 ± 0.03	257.3 ± 0.014	5971.2 ± 0.01	1674	1.86	1.06

Table 4. Relevant Drude Parameters for the Activation Series

sample	ω_P (cm^{-1})	Γ_L (cm^{-1})	Γ_H (cm^{-1})	Γ_X (cm^{-1})	Γ_X (nm)	Q	Q_{Drude}
A1	11668 ± 262	1530 ± 241.5	1589.8 ± 276	9271.6 ± 3319	1078	2.43	2.54
A2	15202 ± 28.6	1301 ± 75.2	4020.1 ± 1406	10925 ± 2792	915	4.02	4.03
A3	16684 ± 51.4	913.3 ± 219.2	5284.1 ± 3403.5	15209 ± 3741	657	4.85	6.30
A4	16017 ± 43.7	1029.9 ± 178.1	4432.2 ± 2714.5	16348 ± 3800	611	4.41	5.64

the crystals. The physics of ionized impurity scattering in metal oxide nanocrystals is reviewed in more detail in ref 38.

Asymmetry in the plasmon line shape can therefore be attributed to frequency-dependent damping of the plasmon and can be confirmed by the damping parameters extracted by fitting our experimental spectra with the modified Drude model (Figure 5a and Table 3). All samples in the series with uniform dopant distribution have a crossover frequency near or just to the red of the LSPR and a significantly larger Γ_L than Γ_H, consistent with the expectation for frequency-dependent damping by ionized impurities.

By contrast, the symmetry of LSPRs of the nanocrystals with surface-segregated tin suggests ionized impurity scattering is somehow suppressed in these nanocrystals (Figure 5b and Table 4). The fits to these spectra result in crossover frequencies far to the blue of their LSPR peaks and a lower Γ_L (higher mobility) than found for the uniformly doped nanocrystals, indicating that the resonance is effectively damped by a frequency-independent constant. To confirm this assertion, the same data were also fit with a simple Drude model (i.e., with a fixed damping parameter), which also gave high-quality fits and was able to reproduce spectral line shapes only for the surface-segregated samples (see Supporting Information).

The difference in the optical properties of nanocrystals with uniformly distributed tin dopants and those with surface-segregated tin can also be quantified in terms of the quality factor of the plasmon resonance, $Q = E/\Delta E$, where E is the LSPR energy and ΔE is its optical line width. We observe nanocrystals with surface segregated tin to have Q factors more than a factor of 2 greater than those with uniformly distributed dopants (see Tables 3 and 4). An alternative derivation of Q can be extracted from the Drude fitting, using Γ_L (in units of energy) instead of ΔE. Q_{Drude} is approximately a factor of 2

dx.doi.org/10.1021/ja502541z | J. Am. Chem. Soc. 2014, 136, 7110–7116

smaller than Q for samples with uniformly distributed dopants due to ionized impurity scattering. For samples with surface segregated tin, Q_{Drude} and Q are nearly equivalent. The Q factors for samples A2−A4 are higher than those reported for copper chalcogenide[39] and tungsten oxide[40] nanocrystals and similar or slightly smaller in magnitude than those recently reported for indium-doped cadmium oxide nanocrystals.[9] Thus, these ITO nanocrystals with surface-segregated dopants have among the highest Q reported to date for semiconducting nanocrystals, approaching values found in noble metal nanoparticles.

We propose a simple physical model to interpret the differences in line shape observed in the optical spectra of the two sample series based on tin dopant distribution in ITO nanocrystals. A nanocrystal with uniformly distributed ionized dopant impurities will experience frequency-dependent damping of the electron cloud similar to what is observed in thin film and bulk samples (see Figure 6a). The transition from a low-

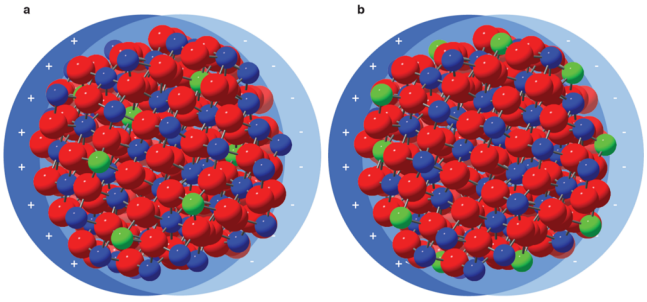

Figure 6. Schematic representation of plasmonic nanocrystals with (a) uniform and (b) surface segregated dopant distributions. When the LSPR is excited, the electron cloud oscillates in response to an external electric field. In panel a, most of the electron cloud is scattered from ionized impurities, pictured in green, whereas in panel b most of the electron cloud is oscillating away from these impurities.

frequency regime with strong damping due to ionized impurities to a high-frequency regime with much weaker damping is expected to occur just to the red of the plasma frequency.[34] These two regimes lead to an asymmetry centered around the LSPR, as observed in the samples with uniform doping.

For a nanocrystal with tin dopants disproportionately concentrated at or near the surface, on the other hand, most of the electron cloud will elude interaction with ionized impurities at all frequencies (see Figure 6b), leading to a near-symmetric line shape. In comparison to the values for a uniform distribution of particles, the fixed damping constant should have a value reflecting scattering in high-quality indium oxide, much smaller than the low-frequency damping constant in uniformly doped ITO. Oxygen vacancy doped indium oxide films most typically have d.c. mobilities on the order of 70−100 $cm^2/V{\cdot}s$,[17,41] with values as high as 160 $cm^2/V{\cdot}s$ reported for high quality crystals. This corresponds to damping parameters less than 1000 cm^{-1}. The values extracted for Γ_L in the surface-segregated samples approach this range, indicating a damping profile for the LSPR that is closer to indium oxide than ITO.

To validate this interpretation of the relationship between dopant distribution and line shape, we simulated the LSPR spectra for nanocrystals with different doping distribution (Figure 5c and d, with more description in the Supporting Information). A uniform distribution yields the expected asymmetry, while nanocrystals composed of an undoped core with a heavily doped shell are predicted to have highly symmetric LSPR spectra. In essence, the surface-segregated dopants donate electrons to the defect-free core where they experience minimal damping. Furthermore, a thinner shell leads to a narrower line shape, with a close approximation to our data for a 0.25 nm shell. This suggests that tin is segregated within the first few atomic layers of the crystal for these samples.

CONCLUSION

We have demonstrated that the dopant distribution has a strong effect on the optoelectronic properties of colloidal ITO nanocrystals. In particular, the activation of dopants and LSPR line shape are correlated to the degree of tin surface segregation. While we suggest on the basis of the literature that oxygen interstitial defects and tin orbital hybridization at or near the ITO surface may be responsible for the observed trends in dopant activation, detailed further experimental and theoretical study will be needed to characterize and understand these defects. Nonetheless, our results suggest that deliberate control over dopant distributions could be used to sculpt the electrostatic landscape experienced by free electrons and thereby tune the optoelectronic properties of plasmonic ITO nanocrystals for targeted applications. For sensing applications,[42−45] where a high quality factor that allows precise tracking of the LSPR frequency and its sensitivity to the surrounding dielectric medium is needed, a narrower and more symmetric line shape may be desirable. On the other hand, applications such as plasmonic smart windows[7,46,47] that require manufacture of nanocrystals with consistent properties across large batches and deployment of devices for decades without performance degradation may require nanocrystals that are less sensitive to dopant compensation in the near surface region; these requirements may be best met by uniformly distributing dopants or even adding an undoped shell. Engineering of dopant distribution presents a new frontier of opportunity for tunable plasmonic materials that is so far accessible only in doped semiconductor nanocrystals.

ASSOCIATED CONTENT

Supporting Information

Details of nanocrystal synthesis, sample characterization by transmission electron microscopy (TEM) and X-ray diffraction (XRD), additional discussion of energy-dependent XPS results, and details of core−shell simulation. This material is available free of charge via the Internet at http://pubs.acs.org.

AUTHOR INFORMATION

Corresponding Author

milliron@che.utexas.edu

Notes

The authors declare no competing financial interest.

ACKNOWLEDGMENTS

The authors acknowledge A. M. Sawvel and T. C. Weng for useful discussions regarding synchrotron data. Work at the Molecular Foundry was supported by the Office of Science, Office of Basic Energy Sciences, of the U.S. Department of Energy (DOE) under Contract No. DE-AC02-05CH11231. Use of the SSRL, SLAC National Accelerator Laboratory, is supported by DOE under Contract No. DE-AC02-76SF00515. S.D.L. and D.J.M. were supported by a DOE Early Career

Research Program grant. E.L.R. was supported by a DOE ARPA-E grant. A.B. was supported by a National Science Foundation Graduate Student Research Fellowship under Grant No. DGE 1106400.

REFERENCES

(1) Naik, G. V.; Shalaev, V. M.; Boltasseva, A. *Adv. Mater.* **2013**, *25*, 3264−3294.
(2) Comin, A.; Manna, L. *Chem. Soc. Rev.* **2014**, DOI: 10.1039/C3CS60265F.
(3) Buonsanti, R.; Milliron, D. J. *Chem. Mater.* **2013**, *25*, 1305−1317.
(4) Radovanovic, P. V. In *Functional Metal Oxides: New Science and Novel Applications*; Ogale, S. B., Venkatesan, T. V., Blamire, M. G., Eds.; Wiley-VCH Verlag GmbH & Co. KGaA: Weinheim, Germany, 2013; Vol. *2013*, pp 163−194.
(5) Felde, U. Zum; Haase, M.; Weller, H. *J. Phys. Chem. B* **2000**, *104*, 9388−9395.
(6) Kanehara, M.; Koike, H.; Yoshinaga, T.; Teranishi, T. *J. Am. Chem. Soc.* **2009**, *131*, 17736−17737.
(7) Garcia, G.; Buonsanti, R.; Runnerstrom, E. L.; Mendelsberg, R. J.; Llordés, A.; Anders, A.; Richardson, T. J.; Milliron, D. J. *Nano Lett.* **2011**, *11*, 4415−4420.
(8) Buonsanti, R.; Llordes, A.; Aloni, S.; Helms, B. A.; Milliron, D. J. *Nano Lett.* **2011**, *11*, 4706−4710.
(9) Gordon, T. R.; Paik, T.; Klein, D. R.; Naik, G. V.; Caglayan, H.; Boltasseva, A.; Murray, C. B. *Nano Lett.* **2013**, *13*, 2857−2863.
(10) Erwin, S. C.; Zu, L.; Haftel, M. I.; Efros, A. L.; Kennedy, T. A.; Norris, D. J. *Nature* **2005**, *436*, 91−94.
(11) Norris, D. J.; Efros, A. L.; Erwin, S. C. *Science* **2008**, *319*, 1776−1779.
(12) Radovanovic, P. V. *Nat. Nanotechnol.* **2009**, *4*, 282−283.
(13) Gilstrap, R. A.; Capozzi, C. J.; Carson, C. G.; Gerhardt, R. A.; Summers, C. J. *Adv. Mater.* **2008**, *20*, 4163−4166.
(14) Choi, S.-I.; Nam, K. M.; Park, B. K.; Seo, W. S.; Park, J. T. *Chem. Mater.* **2008**, *20*, 2609−2611.
(15) Wang, T.; Radovanovic, P. V. *J. Phys. Chem. C* **2011**, *115*, 406−413.
(16) Lee, J.; Lee, S.; Li, G.; Petruska, M. A.; Paine, D. C.; Sun, S. *J. Am. Chem. Soc.* **2012**, *134*, 13410−13414.
(17) Frank, G.; Kostlin, H. *Appl. Phys. A: Solids Surf.* **1982**, *27*, 197−206.
(18) González, G. B.; Mason, T. O.; Quintana, J. P.; Warschkow, O.; Ellis, D. E.; Hwang, J.-H.; Hodges, J. P.; Jorgensen, J. D. *J. Appl. Phys.* **2004**, *96*, 3912−3920.
(19) Hwang, J.-H.; Edwards, D. D.; Kammler, D. R.; Mason, T. O. *Solid State Ionics* **2000**, *129*, 135−144.
(20) Warschkow, O.; Ellis, D. E.; González, G. B.; Mason, T. O. *J. Am. Ceram. Soc.* **2003**, *86*, 1700−1706.
(21) Zarghami, M. H.; Liu, Y.; Gibbs, M.; Gebremichael, E.; Webster, C.; Law, M. *ACS Nano* **2010**, *4*, 2475−2485.
(22) Mendelsberg, R.; Garcia, G.; Li, H.; Manna, L.; Milliron, D. J. *J. Phys. Chem. C* **2012**, *116*, 12226−12231.
(23) Edwards, P.; Porch, A.; Jones, M. *Dalton Trans.* **2004**, 2995−3002.
(24) Mendelsberg, R.; Garcia, G.; Milliron, D. J. *J. Appl. Phys.* **2012**, *111*, 063515.
(25) Yeh, J. J.; Lindau, I. *At. Data Nucl. Data Tables* **1985**, *32*, 1−155.
(26) Sarma, D.; Santra, P.; Mukherjee, S.; Nag, A. *Chem. Mater.* **2013**, *25*, 1222−1232.
(27) Fan, J. C. C.; Goodenough, J. B. *J. Appl. Phys.* **1977**, *4*, 3524−3531.
(28) Cox, P. A.; Flavell, W. R.; Egdell, R. G. *J. Solid State Chem.* **1987**, *68*, 340−350.
(29) Gassenbauer, Y.; Schafranek, R.; Klein, a.; Zafeiratos, S.; Hävecker, M.; Knop-Gericke, A.; Schlögl, R. *Phys. Rev. B* **2006**, *73*, 245312.
(30) Chen, M.; Pei, Z. L.; Sun, C.; Wen, L. S.; Wang, X. *J. Cryst. Growth* **2000**, *220*, 254−262.
(31) Gassenbauer, Y.; Klein, A. *Solid State Ionics* **2004**, *173*, 141−145.
(32) Dong, A.; Ye, X.; Chen, J.; Kang, Y.; Gordon, T.; Kikkawa, J. M.; Murray, C. B. *J. Am. Chem. Soc.* **2011**, *133*, 998−1006.
(33) Hamberg, I.; Granqvist, C. *Appl. Phys. Lett.* **1984**, *44*, 80721−80723.
(34) Hamberg, I.; Granqvist, C. G. *J. Appl. Phys.* **1986**, *60*, 123−159.
(35) Gerlach, E. *J. Phys. C: Solid State Phys.* **1986**, *19*, 4585−4603.
(36) Rech, B.; Ruske, F.; Pflug, a.; Szyszka, B.; Greiner, D.; Sittinger, V. *Thin Solid Films* **2009**, *518*, 1289−1293.
(37) Mergel, D.; Qiao, Z. *J. Phys. D: Appl. Phys.* **2002**, *35*, 794−801.
(38) Lounis, S. D.; Runnerstrom, E. L.; Llordes, A.; Milliron, D. J. *J. Phys. Chem. Lett.* **2014**, *5*, 1564−1574.
(39) Luther, J. M.; Jain, P. K.; Ewers, T.; Alivisatos, A. P. *Nat. Mater.* **2011**, *10*, 361−366.
(40) Manthiram, K.; Alivisatos, A. P. *J. Am. Chem. Soc.* **2012**, *134*, 3995−3998.
(41) Bel Hadj Tahar, R.; Ban, T.; Ohya, Y.; Takahashi, Y. *J. Appl. Phys.* **1998**, *83*, 2631.
(42) Elghanian, R.; Storhoff, J. J.; Mucic, R. C.; Letsinger, R. L.; Mirkin, C. A. *Science* **1997**, *277*, 1078−1081.
(43) Willets, K. A.; Van Duyne, R. P. *Annu. Rev. Phys. Chem.* **2007**, *58*, 267−297.
(44) Larsson, E. M.; Langhammer, C.; Zorić, I.; Kasemo, B. *Science* **2009**, *326*, 1091−1094.
(45) Liu, N.; Tang, M. L.; Hentschel, M.; Giessen, H.; Alivisatos, A. P. *Nat. Mater.* **2011**, *10*, 631−636.
(46) Garcia, G.; Buonsanti, R.; Llordes, A.; Runnerstrom, E. L.; Bergerud, A.; Milliron, D. J. *Adv. Opt. Mater.* **2013**, *1*, 215−220.
(47) Llordés, A.; Garcia, G.; Gazquez, J.; Milliron, D. J. *Nature* **2013**, *500*, 323−326.